Increasing LSPIV performances by exploiting the seeding distribution index at different spatial scales

Silvano Fortunato Dal Sasso[1*], Alonso Pizarro[2], Sophie Pearce[3], Ian Maddock[3],
Salvatore Manfreda[2]

1) Department of European and Mediterranean Cultures: Architecture, Environment and Cultural Heritage (DICEM), University of Basilicata, 75100 Matera, Italy
2) Department of Civil, Architectural and Environmental Engineering, University of Naples Federico II, 80125 Naples, Italy.
3) School of Science and the Environment, University of Worcester, Worcester, UK

*Corresponding author: silvano.dalsasso@unibas.it

Abstract

Image-based approaches for surface velocity estimations are becoming increasingly popular because of the increasing need for low-cost river flow monitoring methods. In this context, seeding characteristics and dynamics along the video footage represent one of the key variables influencing image velocimetry results. Recent studies highlight the need to identify parameter settings based on local flow conditions and environmental factors apriori, making the use of image velocimetry approaches hard to automatise for continuous monitoring. The seeding distribution index (SDI) – recently introduced by the authors – identifies the best frame window length of a video to analyse, reducing the computational loads and improving image velocimetry performance. In this work, we propose a method based on an average SDI time series threshold with noise filtering. This method was tested on three case studies in Italy and validated on one in the UK, where a relatively high number of measurements was available. Following this method, we observed an error reduction of 20-39% with respect to the analysis of the full video. This beneficial effect appears even more evident when the optimisation is applied at sub-sector scales, in cases where the SDI shows a marked variability along the cross-section. Finally, an empirical parameter τ was proposed,

28   calibrated, and validated for practical uses to define the SDI threshold. τ showed relatively stable

29   values in the different contexts where it has been applied. Application of the seeding index to

30   image-based velocimetry for surface flow velocity estimates is likely to enhance measurement

31   accuracy in future studies.

32

33   **Keywords**: Image Velocimetry, UAS, river flow monitoring, LSPIV, seeding metrics, Seeding

34   Distribution Index, frame footage.

1 Introduction

Technological developments, the advent of Unmanned Aerial Systems (UASs), open-source software and smartphone applications – and the increasing need of feasible measurements are promoting the use of image velocimetry techniques for streamflow observations (Manfreda et al., 2018; Eltner et al., 2020). Optical methods allow the estimation of surface velocity in rivers by analysing surface images captured from the banks or above the water surface. The measurement of surface velocity, especially during floods, is a more practical way to derive river flows combining depth-averaged water velocities and cross-sectional area information. The main advantages of using these non-contact technologies concern reducing risk, the low cost of operations, and the possibility of application at inaccessible locations during extreme hydrological events (Le Coz et al., 2010; Boursicaud et al., 2016). Different image velocimetry techniques have been proposed in recent years that use optical images of the stream water surface to derive surface velocity 2D maps (Pearce et al., 2020). These methods include the classical correlation-based algorithms such as Large Scale Particle Image Velocimetry (LSPIV - Fujita et al., 1998) and Large Scale Particle Tracking Velocimetry (LSPTV - Brevis et al., 2011), but also new approaches of optical flow based on the detection of patterns of image intensity, such as Space-Time Image Velocimetry (STIV - Fujita et al., 2007), Surface Structure Image Velocimetry (SSIV - Leitão et al., 2018), Optical Tracking Velocimetry (OTV - Tauro et al., 2020) and Kanade–Lucas Tomasi Image Velocimetry (KLT-IV - Perks 2020). All these methods have been successfully applied on images acquired from both fixed and mobile platforms (UAS) allowing the reconstruction of instantaneous flow velocity fields and the estimation of surface velocity in rivers with errors less than 20% (Kim et al., 2008; Le Coz et al., 2010; Detert et al., 2017; Kintzel et al., 2019; Eltner et al., 2020).

58   Similarly, recent advancements in topographic surveys with modern portable GPS, laser profilers,

59   radar systems, and Structure-from-Motion (SfM) photogrammetry has enabled the acquisition of

60   bathymetry and water depth in a more efficient way (Kintzel et al., 2019; Manfreda et al., 2019a).

61   Remarkably, stream flows can be optically estimated as well when river bathymetry and a vertical

62   velocity profile are known. In this direction, Bandini et al. (2020) recently explored the novel idea

63   to estimate river discharge using both the Manning equation and mid-section method equation

64   relying on bathymetry knowledge, surface velocity measurements from UAS, and water surface

65   slope calculation.

66   However, although these approaches are rapidly increasing, the errors and uncertainty in the use

67   of these methods persist. On the one hand, image velocimetry techniques employ parameters and

68   settings that require a detailed level of expertise (e.g., interrogation area size, cross-correlation

69   parameters). These parameters are related to the specific field conditions – such as seeding density,

70   tracers' dimension, frame rate, flow velocity itself – and are not easily identifiable. Pearce et al.

71   (2020) performed a sensitivity analysis to identify the best setting configuration for different

72   optical techniques. Rozos et al., (2020) suggested a statistical approach to overcome the

73   subjectivity of the selection of the parameter settings exploring the impact of parameter uncertainty

74   on the results of the image velocimetry methods. On the other hand, the efficiency of these methods

75   can be influenced by environmental factors (e.g., wind, light reflection and shadows), local

76   hydraulic conditions (e.g., flow regime, flow velocity and directions), and operational practises

77   (e.g., seeding deployment, camera movements) (Muste et al., 2008, Kim et al., 2008; Tauro et al.,

78   2017). We have recently shown that the dynamics on time of seeding characteristics showed

79   statistical significance on image-based performances (Dal Sasso et al., 2020). With respect to

80   seeding conditions, the image velocimetry application by detecting and matching natural features

81 (turbulence ripples, differences in colour due to suspended sediments and natural debris) still

82 remains a challenge. Generally, the deployment of artificial tracers is necessary to improve these

83 methods' accuracy (Detert et al., 2017).

84 Moreover, the number of frames to analyse is still an issue. A systematic reduction of errors is

85 observed in numerical experiments (Manfreda et al., 2019b) and laboratory flumes (Samarage et

86 al. 2012) by increasing the number of frames. This evidence is due to the fact that a higher number

87 of frames increases the number of velocity samples in space and can help to smooths out outliers

88 and noise with a consequent reduction of errors (Pizarro et al., 2020a and 2020d). This effect is

89 particularly evident for low seeding conditions and where particles are not uniformly distributed

90 over the entire frame sequences. However, this beneficial effect is not always observed in natural

91 environments, where considering a large number of frames leads to increasing the occurrences of

92 possible environmental disturbances over the video sequence (e.g., camera movements,

93 environmental noise). For instance, Strelnikova et al. (2020) observed that a significant increase

94 in the number of processed image pairs might negatively influence ensemble correlation results,

95 significantly increasing the computational costs. Pizarro et al. (2020d), in their field experiments,

96 showed that the use of a long frame sequence has no significant influence for improving final

97 results. Moreover, intense computational times and hardware sources are needed to analyse and

98 store long video time series. The processing time increases as a function of the number of frames,

99 the extension of the Region of Interest (ROI), and the number of features detected (Perks, 2020).

100 For this reason, generally, a reference sequence of frames in which tracers are visible is arbitrarily

101 selected and extracted for image velocimetry processing.

102 In this regard, Pizarro et al. (2020a and 2020b) recently introduced the Seeding Distribution Index

103 (SDI) as a parameter that synthesises the seeding conditions in the field, merging seeding and

104   spatial distribution characteristics. This dimensionless index was formulated using numerical

105   experiments and tested in some field case studies for describing the heterogeneous spatial

106   distribution of tracers and the tendency to form clusters. The evidence shows that this index can

107   be a good descriptor for identifying the portion of the video with the best seeding condition and

108   consequently, can be useful to improve image velocimetry performance.

109   Considering these issues and these recent findings, there is an overall need to harmonise these

110   techniques for the scientific community, technicians, and practitioners to obtain more accurate

111   surface flow velocity estimations. For this purpose, Perks at al. (2020a) collected different field

112   experiences placed in six countries in which streamflow measurements were performed using fixed

113   or mobile cameras (mounted on drones) coupled with image velocimetry techniques. This was a

114   successful trial to test setting parameters, new algorithms, and establish practical guidelines of

115   surface velocimetry estimations form optical cameras.

116   Applying the outcomes of these recent studies, this work investigates a possible strategy for

117   minimising the errors in surface velocity estimations identifying the best frame window based on

118   the characteristics of seeding in space and time. For this purpose, this work explored the possibility

119   of applying image velocimetry techniques at the scale of the entire cross-section (sector) and at the

120   local scale (sub-sectors) to improve the quality of the optical estimations. Moreover, a unique

121   empirical parameter, calibrated on three case studies and validated on a further, was derived. It can

122   represent a comprehensive reference to calculate SDI threshold with only a knowledge of seeding

123   density and independently from field experiments' specific characteristics.

124   2   Field case studies and image data

125   In this work, three different case studies were analysed to identify a unique empirical SDI threshold

126   and isolate the best frame footage for optimising image-based surface velocity estimates. The

127   calibration dataset includes measurements performed on three field case studies at the Brenta,

128   Noce, and Bradano rivers in Italy. A further case study, acquired on River Arrow in the UK was

129   considered as a validation site. The choice of these field experiments incorporated the homogeneity

130   of benchmark methods for surface velocity estimation (current meters), the presence of a high

131   number of measurements, and a wider range of seeding conditions. Figure 1a shows the different

132   case studies' location and presents an example of the original grayscale frame for each case study

133   (Figure 1b - e). The main hydraulic and experimental settings are well documented in Perks et al.,

134   (2020b) and synthesised in Table 1.
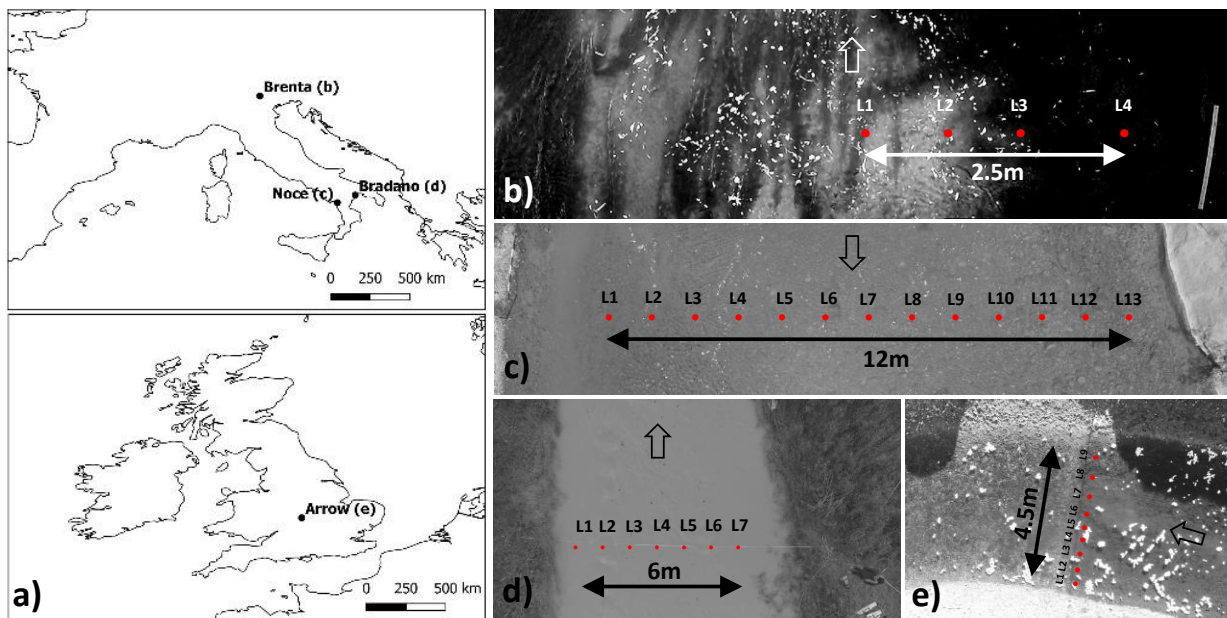
135
136   Figure 1. a) Location of each case study with examples of frames captured with the indication of cross-section width monitored and measurement
137   locations (red circles) distinguished in calibration dataset (b) Brenta river, Italy; c) Noce river, Italy; d) Bradano river, Italy) and e) validation dataset
138   (Arrow river, UK).

139
140   The Brenta river campaign was carried out by Tauro et al. (2017) using a GoPro Hero3+ black

141   edition camera mounted on a pole on the downstream side of a bridge and with a resolution of

142   1920x1080 px. The calibration factor from pixels to meters was estimated as 0.005 m/px.

143   Reference measurements were acquired in-situ with an OTT Hydromet C2 current meter at four

144   locations along the stream cross-section (see Fig. 1b). During the experiment, ten separate 20-

145   second videos at 25 fps were recorded. However, due to some significant disturbances at the right

146   side of the cross-section (light reflections on the water surface), the videos considered for this

147   analysis were restricted to the first five sequences.

148   On the Noce river, Basilicata region (Italy), images were collected from a DJI Phantom 3 Pro UAS

149   (Dal Sasso et al., 2018). A total of 400 consecutive images with a resolution of 1920x1080 px and

150   a frame rate of 24 Hz were considered for the analysis. The ground sampling distance (GSD) was

151   0.009 m/px. Velocity measurements were acquired with a Seba F1 current meter at 13 locations

152   spaced 1 m (see Fig. 1c).

153   The third case study is located in Bradano River, Basilicata region (Italy). Video footage was

154   captured from a DJI Phantom 3 Pro UAS for 1 min 43 s at a pixel resolution of 1920x1080 px, and

155   a frame rate of 24 Hz. Transformation of the images from pixel units to real metric world

156   dimensions can be achieved using the following relationship: 1 px = 0.009 m. Benchmark

157   velocities were obtained at seven points in the cross-section, at 1m intervals, using a Seba F1

158   current meter (see Fig. 1d).

159   The River Arrow represents the case study considered for validation purposes which was acquired

160   in Warwickshire, UK. Video footage was acquired using Phantom 4 Pro UAS with a pixel

161   resolution 1920x1080 px and frame rate 30 Hz. The pixel dimensions of the processed imagery

162   are 0.0096 m in the x and y axes. Reference measurements were obtained through a Valeport 801

163   electromagnetic current meter for two cross-sections within nine individual measurements with a

164   spacing of 0.5 m between each (see Fig. 1e). The cross-section considered for the SDI and image

165   velocimetry analysis was located upstream of the river bend. The latter has been done to minimise

166   the effect of the bend on river velocity calculations.

167
168 *Table 1. Main flow characteristics at monitored cross-sections with the description of image-based and current meter systems used for velocimetry purpose.*

Case Study	Contributing Area [km^2]	Mean surface velocity [m/s]	Maximum surface velocity [m/s]	River discharge [m^3/s]	Image System	Benchmark measurements (n. locations)
Brenta (Italy)	252	0.38	0.46	2.76	fixed (bridge)	Current meter OTT Hydromet C2 (n.4)
Noce (Italy)	413	0.43	0.48	1.70	mobile (UAS)	Current meter SEBA F1 (n.13)
Bradano (Italy)	2581	0.82	1.47	3.97	mobile (UAS)	Current meter SEBA F1 (n.7)
Arrow (UK)	94	0.24	0.27	1.46	mobile (UAS)	Current meter Valeport 801 (n.9)

169
170 For all the case studies, artificial seeding was manually deployed on the free surface upstream of

171 the river reach monitored. In particular, wood chips were used on Brenta and Noce rivers, charcoal

172 tracers on Bradano river, and eco foam chips on the River Arrow. Moreover, the discharge was

173 calculated by applying the velocity-area method at velocity profiles sampled in the cross-sectional

174 flow area (Herschy, 1985).

175 **3 Materials and methods**

176 For all the case studies, nadir videos were acquired with the camera's y-axis orthogonal to the flow

177 direction. Therefore, no algorithm for orthorectification (distortion correction) was applied.

178 However, videos captured by UAS were pre-processed to minimise the apparent movement of the

179 platform. The stabilisation algorithm used consists of an automatic feature selection method that

180 identifies features in frame pairs, matching them to compute possible camera movements (Dal

181 Sasso et al., 2020, Pizarro et al., 2020a). The conversion between pixel units and metric units were

182 done using Ground Control Points (GCP) targets or reference objects located in the field.

183   Videos were acquired at 24-30 frames per second (fps), and frames were extracted and resampled

184   according to the average surface velocity measured in the field. The resampling is useful to

185   enhance the particle displacement with respect to the tracer dimension and reduce computational

186   time. In particular, for the Brenta river, the same frame rate used by Tauro et al. (2017) was

187   adopted, which is 12.5 fps leading to a total number of 2500 frames to be analysed. The Noce river

188   dataset was resampled at 12 fps according to the authors' analysis for a total of 400 frames (Dal

189   Sasso et al., 2018). For the River Arrow, from the recordings, a dataset of 799 consecutive images

190   (sampled at a frame rate of 5 Hz) were extracted for image velocimetry purposes. No resampling

191   process was performed on the Bradano river because of the higher surface velocities measured in

192   the field; therefore, the frame sequence comprised a total of 2496 frames.

193   The frames extracted were converted in grayscale intensity and pre-processed using binarisation

194   to enhance lighter particles' visibility against a dark background as is required by the seeding

195   metric tool (Pizarro et al., 2020). Binarisation by thresholding converts the grayscale image (pixels

196   values between 0 and 255) to an image with pixel values of 0 and 1, by changing the foreground

197   pixels to white and background pixels to black. To this aim, the binarisation threshold selected

198   ranged between 80% and 90% of 255 (8 bits). A higher threshold (90%) was considered for the

199   River Arrow because of the significant presence of light reflections during the frame footage. Table

200   2 contains all the video characteristics used for image-based analyses.

201   *Table 2. Main video characteristics after pre-processing.*

Case Study	GSD [m/px]	fps	Number of Frames	Binarisation [%]
Bradano (Italy)	0.009	24	2496	80
Brenta (Italy)	0.005	12.5	1250	80
Noce (Italy)	0.009	12	200	80

| Arrow (UK)	0.0096	5	799	90

202

203 Afterwards, for each case study, the Seeding Distribution Index (SDI) (Pizarro et al. 2020a and

204 2020b) was calculated frame by frame and an SDI time series were produced. SDI is defined as:

$$SDI = D^{*0.1} / \left(\frac{\rho}{\rho_{cD^*1}} \right), \tag{1}$$

205 where $D^*, \rho,$ and ρ_{cv1} are the empirical spatial clustering level of tracers, the seeding density, and

206 the converging seeding density at the Poisson case (D*=1), respectively. ρ_{cD^*1} was estimated as

207 1.52E-03 particles per pixel (ppp) in Pizarro et al. (2020), whereas D* is computed as

208 [Var(N)/E(N)], where Var(N) and E(N) are the spatial variance and mean value of the number of

209 tracers N computed on subsectors of the same dimensions. It is critical to underline that SDI

210 showed a strong positive correlation with velocimetry errors. Therefore, it can be used as a proxy

211 to select the best set of images for image velocimetry applications.

212 The spatial distribution of tracers varies significantly along the cross-section producing different

213 seeding configurations in time and space. This variability depends on different aspects: the

214 hydrodynamic characteristic of the flow, the morphological characteristics of the river reach, the

215 type and amount of material deployed, and the number and experience of operators. For this reason,

216 SDI time-series calculations and LSPIV analyses were performed at the cross-section scale (sector

217 scale) and at sub-portions (sub-sector scale), as illustrated in Figure 2. Different Region of Interests

218 (ROIs) were identified, consisting in one sector covering the entire transect of benchmark

219 measurements and two sub-sectors of the same dimension, located in the left (LH) and right (RH)

220 part of the cross-section. In particular, the ROI was schematised as a rectangle with one size equal

221 to benchmark measurements (along the cross-section) and the other size of 1m (along the flow

222 direction). For the Bradano river case study, a more extended ROI was considered (about 4m in

223 the flow direction) to allow statistical analysis inside the ROIs because of the low seeding

224   conditions. Figure 2 shows a schematic representation of the cross-section of the Bradano river

225   with the entire sector and two sub-sectors considered for the analysis.
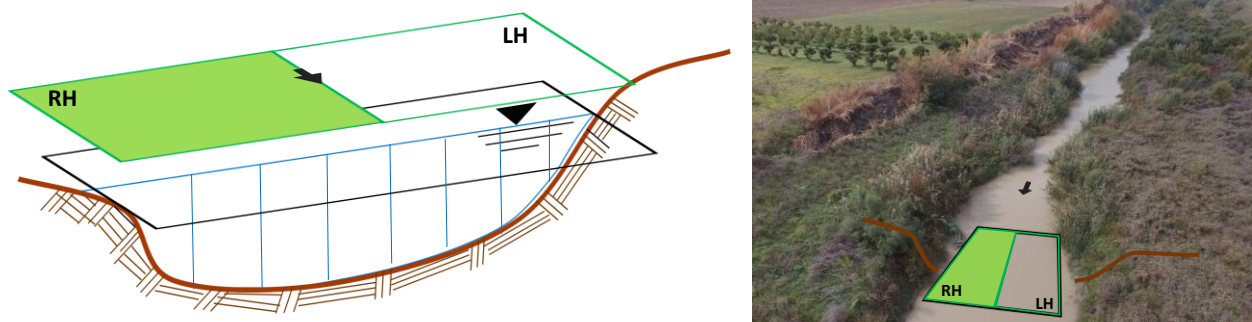
226

227   *Figure 2. Schematic representation of cross-section on Bradano river (Italy) with an indication of the sector (black box) and sub-sectors (green*
228   *boxes) for the SDI calculations and image velocimetry analysis.*

229   Starting from SDI time-series calculations (Figure 3a), a smoothing function was applied to the

230   SDI time series to reduce the noise. This function uses the moving average filter that smooths data

231   by replacing each data point with the average of the neighbouring data points defined within the

232   span of 10 frames (Figure 3b). The filtered SDI time-series average value was considered a

233   threshold to identify the best video portion to analyse. The used criteria are based on: *1)* the

234   identification of frames with an SDI index lower than the average threshold; *2)* the selection of the

235   best frame window (FW) that maximises the number of frames; and if more than one FW assures

236   1 and 2, a further criterion applies. This criterion relies on the minimisation of the SDI averaged

237   within the frame window (Figure 3c)".

238
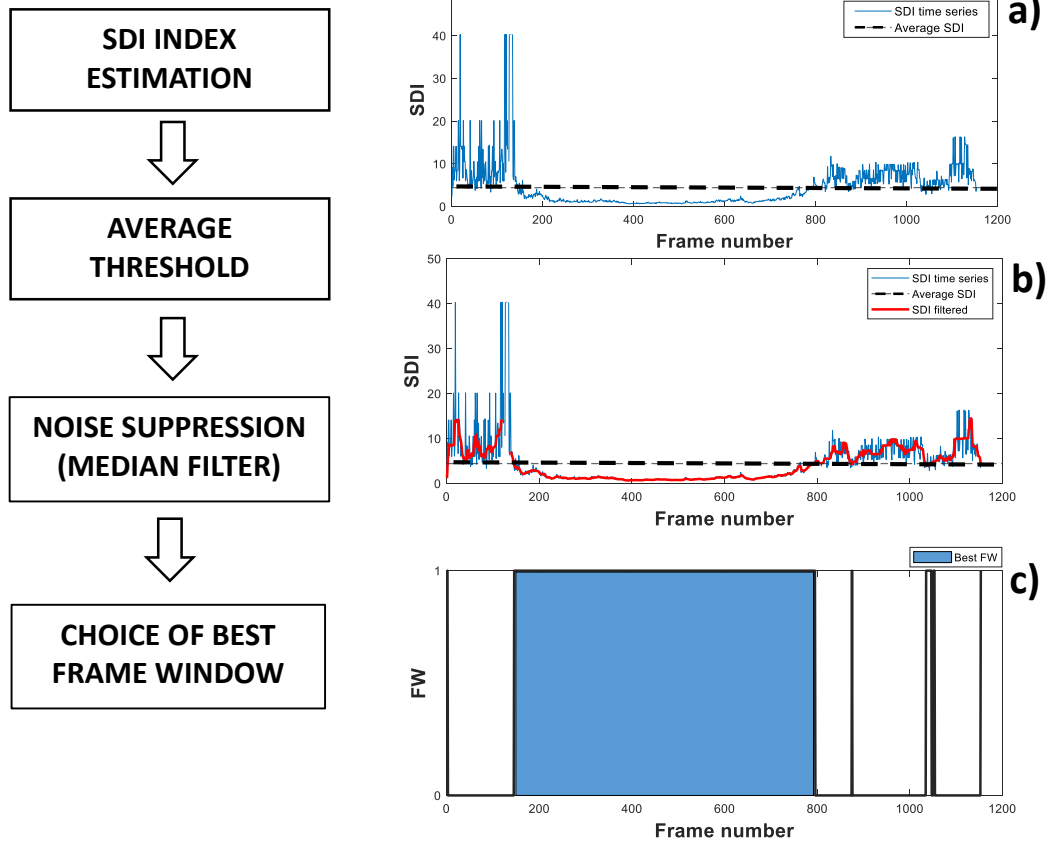
Figure 3. The methodology used includes the following three steps: a) SDI time series and average SDI calculation (dashed line); b) SDI filtering (red line); c) individuation of the best frame window (light blue box).

241

242 LSPIV analysis was carried out using the PIVLab software (Thielicke and Stamhuis, 2014), an

243 open-source toolbox for image velocimetry analysis developed in Matlab. The LSPIV algorithm

244 was applied using the Fast Fourier Transform (FFT) with a three-pass standard correlation method

245 (search and interrogation areas of 128×64, 64×32, and 32×16 px). Additionally, the 2×3-point

246 Gaussian fit was employed to estimate the sub-pixel displacement peak. This method fits a one-

247 dimensional Gaussian function to the discrete intensity distribution of the correlation matrix to

248 determine the sub-pixel particle displacement. The images were analysed adopting the sequencing

249 style 1–2, 3–4. This choice led to optimising the analysis for video sequences (e.g., Brenta river)

250 in which non-consecutive frames between videos were available. Moreover, no post-processing

251 method was applied to filter erroneous velocity results.

252   The performance of LSPIV results was determined by comparing for each measurement location

253   (i) the computed velocities with the current meter measurements considering only the component

254   of velocity in the flow direction (U). Velocity values of each location represent the average of

255   velocity estimated in a square with sides of 0.30 m centred on the measured point (Dal Sasso et

256   al., 2018).

257   The Absolute Percentage Error, APE_i (where i refers to the generic measurement location) was

258   calculated as:

259    $$APE_i = \left| \frac{(U_{Ci} - U_{Ri})}{U_{Ri}} \right| \% \,, \tag{2}$$

260   where U_{Ci} is the computed velocity and U_{Ri} is the reference velocity.

261   For each case study, the index *MAPE* (Mean Absolute percentage error), that is the mean of all the

262   APE_i, was calculated as:

263    $$MAPE = \frac{1}{n}\sum_{1=1}^{n} APE_i = \frac{1}{n}\sum_{1=1}^{n} \left| \frac{(U_{Ci} - U_{Ri})}{U_{Ri}} \right| \% \,, \tag{3}$$

264   where *n* refers to the total number of measurement locations.

4 Results

266   In this section, we report the results of the application of the method illustrated previously. We

267   first present the SDI calculation for each case study at sector and sub-sector scales identifying the

268   frame window (FW) that satisfies the criteria described in Section 2.2. Then, we show the image

269   velocimetry results obtained by analysing all video data available and the best frame window

270   identified after SDI calculation. A unique empirical threshold is identified and applied to a

271   validation case study to test the benefits of the method proposed. Finally, we compare the velocity

272   estimations from LSPIV to the benchmark measurements at different local scales to estimate mean
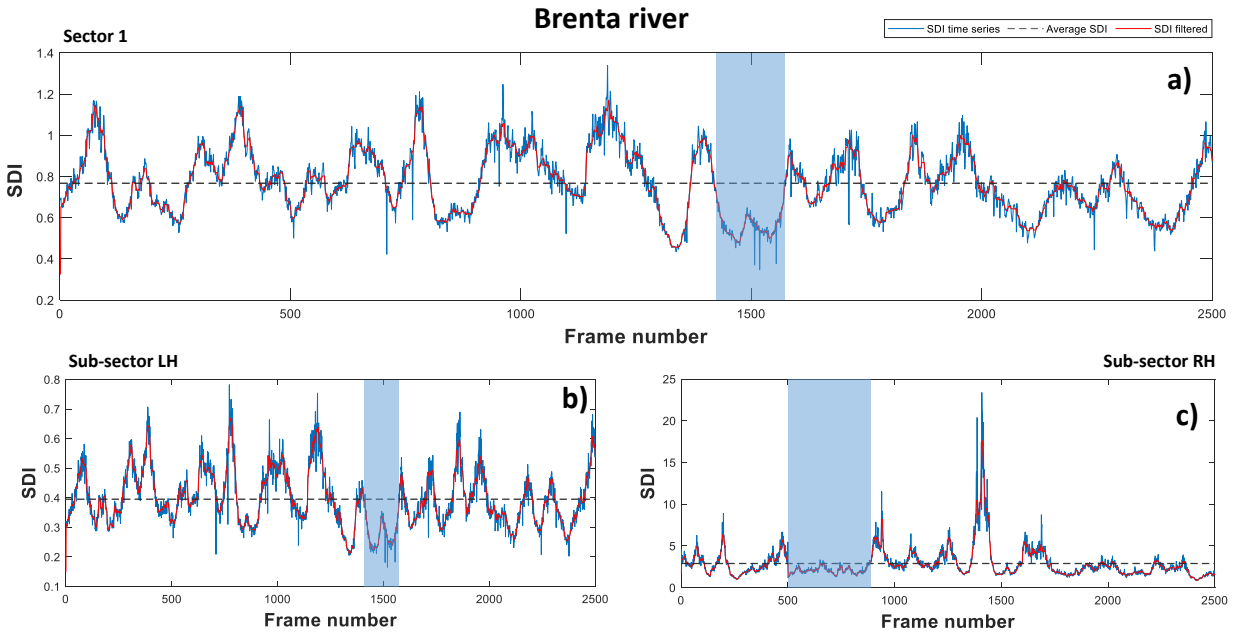
273   absolute errors.

4.1 SDI time series analysis

Figure 4 shows an overview of the dimensionless SDI index calculated for the entire ROI and two sub-sectors, located on the left (LH) and the right part (RH) of the cross-sections, respectively. Note that LH and RH are defined considering the flow direction.
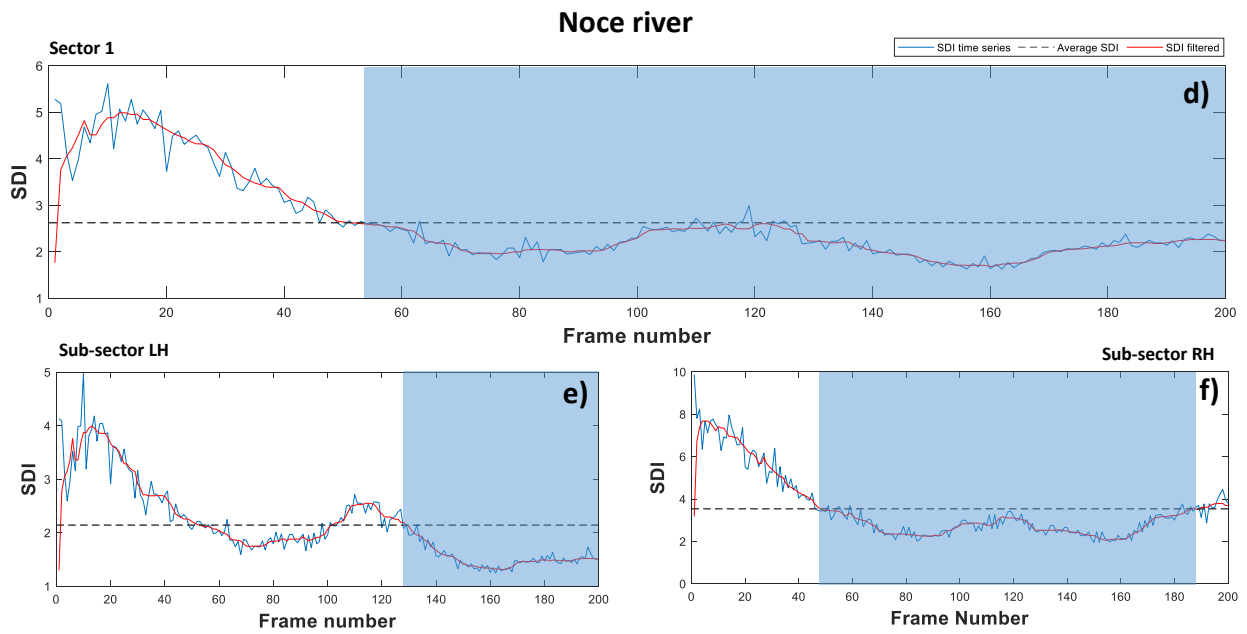
The Brenta river presented the highest seeding density values (2.75E-03 ppp) and spatial distribution of tracers (14.31). The behaviour of the SDI along the frame footage was very stable (between 0.35 and 1.34) especially in the left part of the cross-section similar to the entire sector (Figure 4 a,b). On the contrary, the SDI time series referred to the RH sub-sector showed a different behaviour due to the lower seeding density that reached an average value of 7.93E-04 ppp (Figure 4c). On the Noce river, the average seeding density calculated was 7.70E-04 ppp, and the spatial distribution of tracers was 6.96. The SDI values along the video footage were more consistent and showed the highest variability (between 1.63 and 5.61). On the Brenta river, the behaviour of the SDI in the left part of the cross-section was similar to the entire sector while in the right sub-sector was quite different (Figure 4d,e,f). The Bradano River had the lowest seeding values (6.89E-05) and the dispersion of tracers (2.80). As showed in Figure 4g, the SDI values showed the highest variability (between 7.19 and 390.24). This variability was particularly evident in the left part of the cross-section where the lack of seeding did not allow the calculation of SDI values for different frames in the last part of the video (Figure 4h).

Brenta river
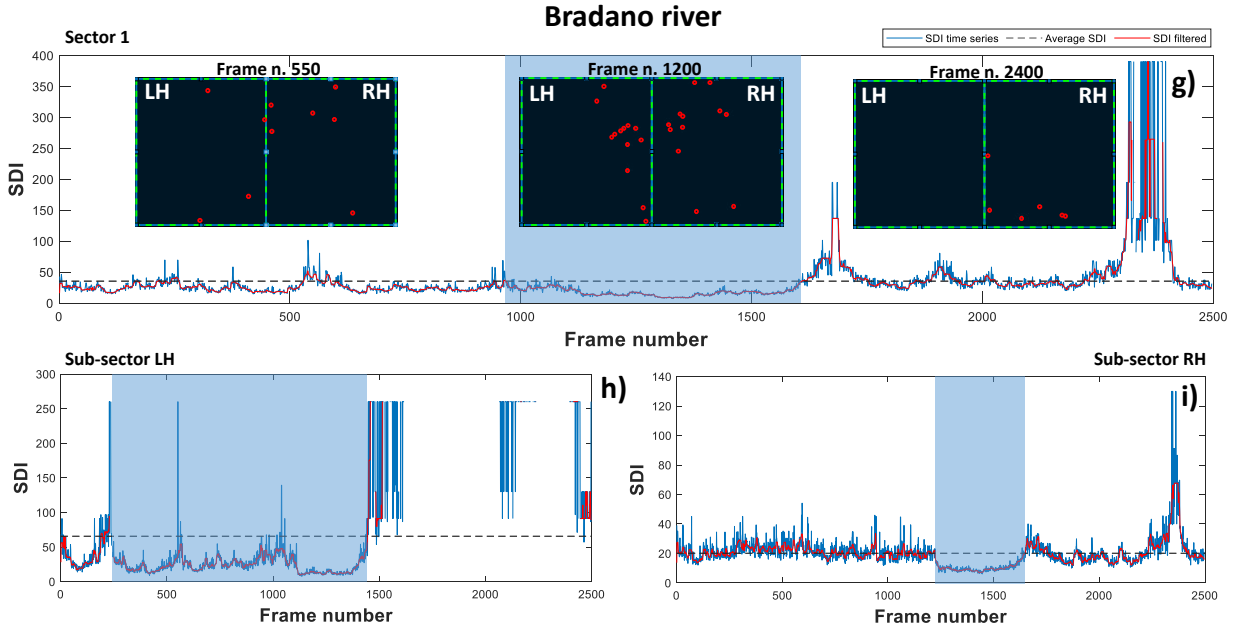
Sector 1

a)

Sub-sector LH

b)

Sub-sector RH

c)

294

Noce river

Sector 1

d)

Sub-sector LH

e)

Sub-sector RH

f)

295

Figure 4. SDI times series calculated at sector and sub-sectors scales (LH and RH are the left-hand and right-hand subsectors) with the indication of the SDI threshold (dashed line) and best frame window (light blue box) for a,b,c) Brenta river; d,e,f) Noce river; and g,h,i) Bradano river, respectively. The red line represents the filtered SDI time series.

Table 3 presents the average values of seeding density ($\bar{\rho}$), dimensionless dispersion index ($\bar{D}^*$), and SDI threshold for each case study at the sector and sub-sectors scales. Moreover the $\tau = \rho_{cD*1}\bar{D}^{*0.1}$ parameter was calculated. It is worth noting that τ represents a key factor to derive the SDI threshold using only seeding density information. We observed that on average this parameter stabilised around 0.002 ppp when tracers transit in the field of view for the different case studies considered in this work. In contrast, it increased when the video footage includes frame sequences without seeding (e.g. Bradano, LH sub-sector).

Table 3. Average seeding characteristics, expressed in terms of average seeding density ($\bar{\rho}$), spatial distribution of tracers ($\bar{D}^*$), SDI threshold and parameter (τ), calculated at sector and sub-sector scales for the calibration dataset.

River	Number of sectors		$\bar{\rho}$ [ppp]	$\bar{D}^*$ [-]	SDI threshold [-]	τ [ppp]
Brenta		1	2.75E-03	14.31	0.77	0.0021
	2	LH	4.98E-03	7.06	0.36	0.0018
		RH	7.93E-04	7.12	2.89	0.0023
Noce		1	7.70E-04	6.96	2.62	0.0020

	2	LH	9.52E-04	7.02	2.14	0.0020
		RH	5.91E-04	6.18	3.54	0.0021
Bradano		1	6.89E-05	2.8	30.72	0.0021
	2	LH	5.00E-05	2.17	60.72	0.0030
		RH	9.42E-05	2.28	20.99	0.0020

4.2 Image velocimetry results

Table 4 presents the summarised information about the comparison of LSPIV velocity estimates

and the current meter measurements for each case study. MAPE is presented for the different

configurations that include the analysis considering all the frames and adopting the optimal frame

window for one sector and two sub-sectors. The error reduction, expressed in terms of MPE,

obtained using the best frame window with respect to the entire video configurations are reported

in brackets, for both one and two sectors. Appendix A synthesises, for each case study, the

following information: a reference pre-processed image with the indication of current meter

measurements (L_i) and the two sub-sectors (LH and RH), the reference surface velocities, and

absolute percentage error APE (%) calculated for each location considered in the analysis.

For all the case studies, a reduction of absolute percentage error was found by employing the

optimal frame window that minimises SDI at different spatial scales. In particular, on the Brenta

river, the MAPE considering all the available frames (n=2500) was equal to 14.26%; moving on,

the best frame window in the sector (n=154 frames) stabilised around 13.92% with an error

reduction of 2%. The restricted number of frames considered for the LSPIV analysis determined

an improvement of the results on the left side (locations L1 and L2) compared to the right side

characterised by a lower seeding density (see location L3, see Table A1 in Appendix). Considering

the different SDI behaviours inside the two sub-sectors, the LSPIV results stabilised with an error

of around 10.88%, leading to an overall error reduction of 24%. On the Noce river, MAPE was

14.28% considering all the frames available (201). Despite the low number of frames analysed,

330   the high seeding density allowed the selection of an optimised frame window to improve the final

331   results on both the sector and sub-sector scales. The errors calculated using the best FW in one

332   sector and two sectors were 11.44% and 9.92% with an error reduction of 20 and 31%,

333   respectively. On the Bradano river, the high number of frames allowed the applicability of the

334   methodology in extremely low seeding conditions. The average absolute error computed using all

335   frames (n=2496) was 12.23%, whereas considering the best frame window at one sector was 9.34%

336   with a reduction of 24%. No significant improvement was found using the best frame window at

337   sub-sector scales (11.06%). The latter can be explained by the limited number of frames analysed

338   in the right portion of the cross-section because of the lower seeding density and sampled velocity

339   vectors which are not enough to reconstruct the velocity field accurately.

340

341   *Table 4. Overview of average absolute errors calculated considering all the frames and the best frame windows over the entire ROI and sub-*
342   *sector scales. Values in parenthesis represent the reduction of error in percentage respect to the configuration adopting all frames on the entire*
343   *ROI or specific sector, respectively.*

River	Sectors	Number of frames n	Frame window	MAPE [%]	
Brenta	1	2500	entire video	14.26%	
	1	154	1420-1573	13.92% (-2%)	
	2-LH	2500	entire video	13.30%	
	2- RH	2500	entire video	15.22%	
	2-LH	154	1420-1573	7.26% (-45%)	10.88% (-24%)
	2- RH	379	501-879	14.49% (-5%)	
Noce	1	201	entire video	14.28%	
	1	150	52-201	11.44% (-20%)	
	2-LH	201	entire video	17.40%	
	2- RH	201	entire video	10.63%	
	2-LH	71	130-201	10.07% (-42%)	9.92% (-31%)
	2- RH	124	48-186	9.27 % (-13%)	
Bradano	1	2496	entire video	12.23%	
	1	642	967-1608	9.34% (-24%)	
	2-LH	2496	entire video	15.82%	
	2- RH	2496	entire video	9.84%	
	2-LH	1194	250-1443	10.63% (-28%)	11.06% (-9%)

	2- RH	422	1224-1645	10.28% (+4%)	

344

345   Figure 5 shows the surface velocity maps computed for the three case studies considering the entire

346   video configuration and the best one between one and two sectors. From this figure, it is possible

347   to observe that a good sampling of velocities inside the ROIs is generally obtained also reducing

348   the number of frames processed (e.g., 6% of the total frames in Brenta river). This depends on the

349   SDI behaviour inside the ROI, increasing its influence at low seeding conditions (e.g., Bradano

350   river). Note that a great level of detail is achieved in Figure 5 even with a reduced – but highly

351   informative – number of frames. This idea is validated considering the case study below.
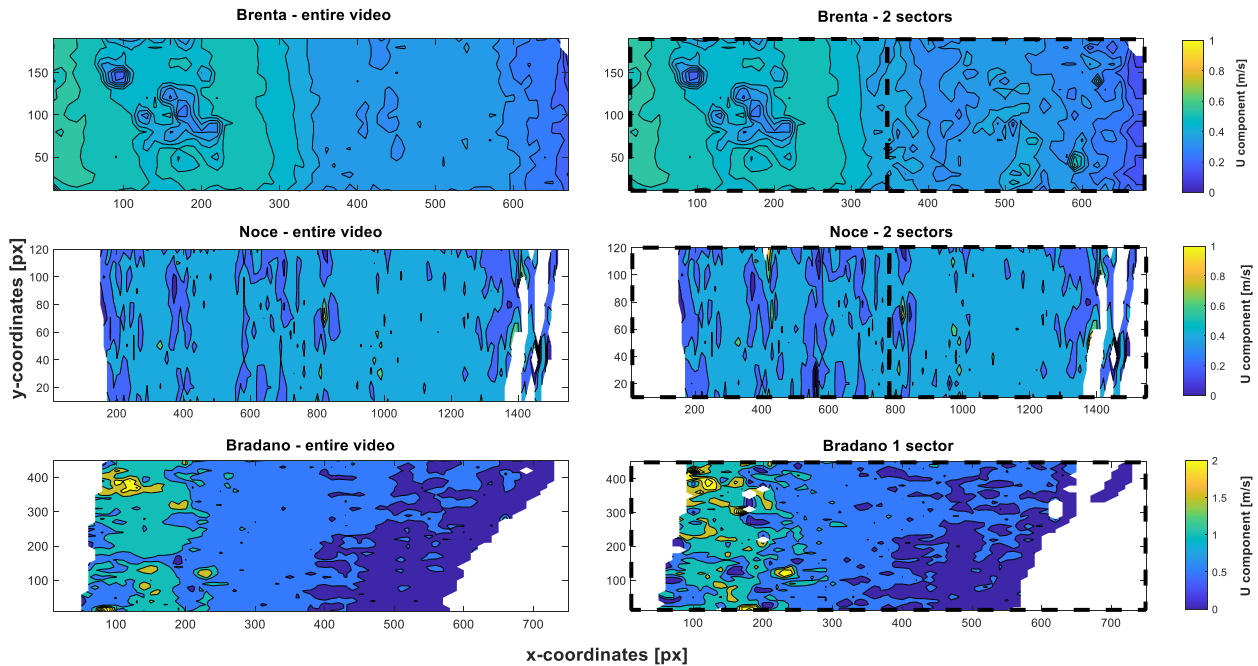
352
353   *Figure 5. Averaged surface velocity maps computed for each study case inside the ROI considering the entire video and the best configuration*
354   *between the entire ROI or two sub-sectors (dashed black boxes).*

355

356   ## 4.3 Validation on the River Arrow

357   The River Arrow dataset, described in Section 2.1, has been used for the validation of the proposed

358   procedure (Figure 6). In particular, the empirical threshold $\tau = 0.002$, calibrated on the other three

359 study cases, was tested to identify the best temporal frame window for image-velocimetry

360 analyses. The River Arrow case study showed high average seeding density (7.37E-04 ppp) and

361 low dispersion of tracers in the field of view (2.72).

362

363 *Figure 6. River Arrow with the indication of the cross-section monitored upstream the bend and the two ROIs considered for the analysis.*

364 The seeding behaviour was similar inside the different sectors because of the homogeneous

365 distribution of tracers on the mid-cross-section (Figure 7a, b, c). However, more noise effect was

366 visible in the sector in the right part of the cross-section (Figure 7c). Considering the parameter

367 $\tau = 0.002$ ppp and the reference seeding density for each sector, the calculated SDI thresholds were

368 equal to 2.71 (sector 1), 1.82 (sub-sector LH) and 3.70 (sub-sector RH).
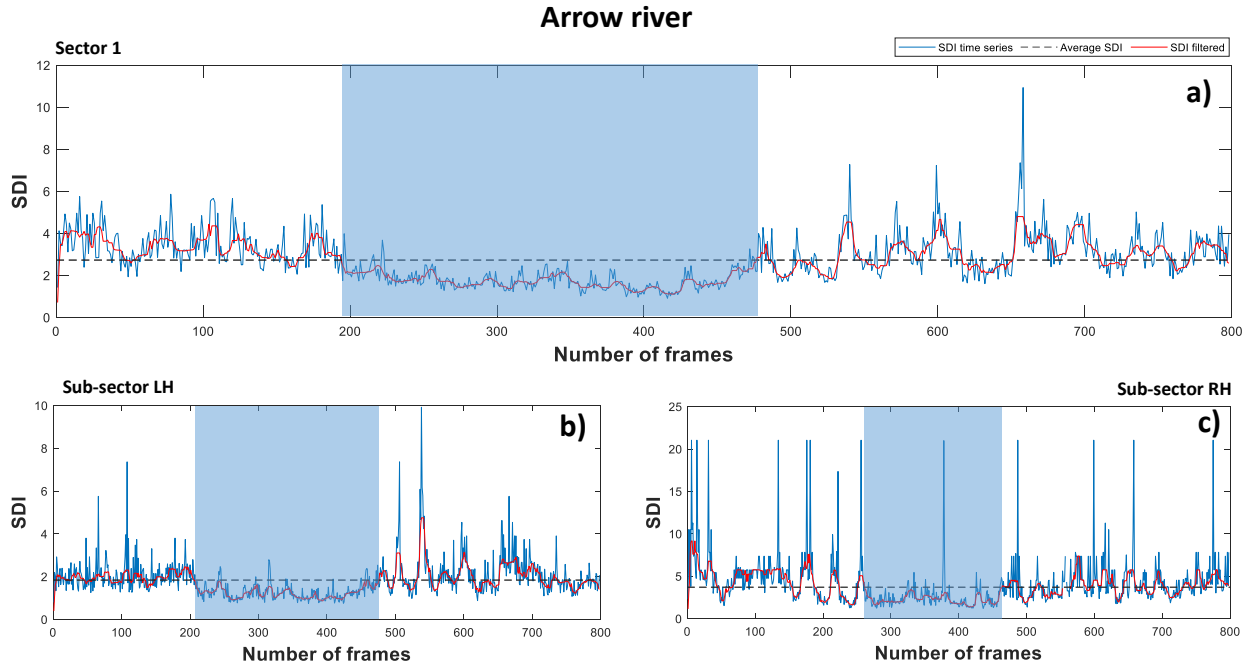
Figure 7. SDI time series calculated on Arrow river at sector and sub-sectors scales (LH and RH) with the indication of SDI threshold (dashed line) and best frame window (light blue box).

These thresholds allowed the identification of the best frame windows within the video footage and image velocimetry analysis was performed using only these frames (Table 5). The mean absolute percentage error computed using all frames available (n=798) over the entire ROI was 12.37%; whereas using the best frame window (n=282) the error reduced by around 7.59%. In the present case, the analysis performed on the two subsectors was not able to identify a significantly different set of frames. For this reason, the error was similar to the one performed over the entire ROI with an error of around 8%. This is due to the fact that seeding distribution is quite uniform in space.

Figure 8 shows the surface velocity map computed considering the entire video and the optimal frame window. It is possible to observe that the homogeneous seeding conditions allowed to obtain a full velocity map with a significantly reduced error using about 35% of the total number of frames. In the present case, the optimal velocity map retained was the one estimated over the entire

385   ROI, because we measured an increase in errors on the right sector with respect to the current

386   meter. It is worth noting the error in the two subsectors obtained using the optimal set of frames is

387   below 8.4%, while the same result obtained including all frames shows a variability from 5.15%

388   up to 19.63 %. Notwithstanding the uncertain reliability of the current meter data, it is important

389   to acknolwedge the results obtained on the two subsectors provide a more stable result, which

390   opens the possibility of improving image velocimetry methods' reliability and accuracy.

391   *Table 5. Average absolute errors calculated considering all the frames and the best frame windows over the entire ROI and sub-sector scales*
392   *for the River Arrow. Values in parenthesis represent the reduction of error in percentage respect to the configuration adopting all frames on the*
393   *entire ROI or specific sector, respectively.*

River	Sectors	Number of Frames	Frame Window	MAPE [%]	
Arrow	1	798	entire video	12.37%	
	1	282	195-476	7.59 (-39%)	
	2-LH	798	entire video	19.63%	
	2- RH	798	entire video	5.15%	
	2-LH	270	206-475	8.16% (-58%)	8.01 (-33%)
	2- RH	202	262-463	8.37% (+62%)	
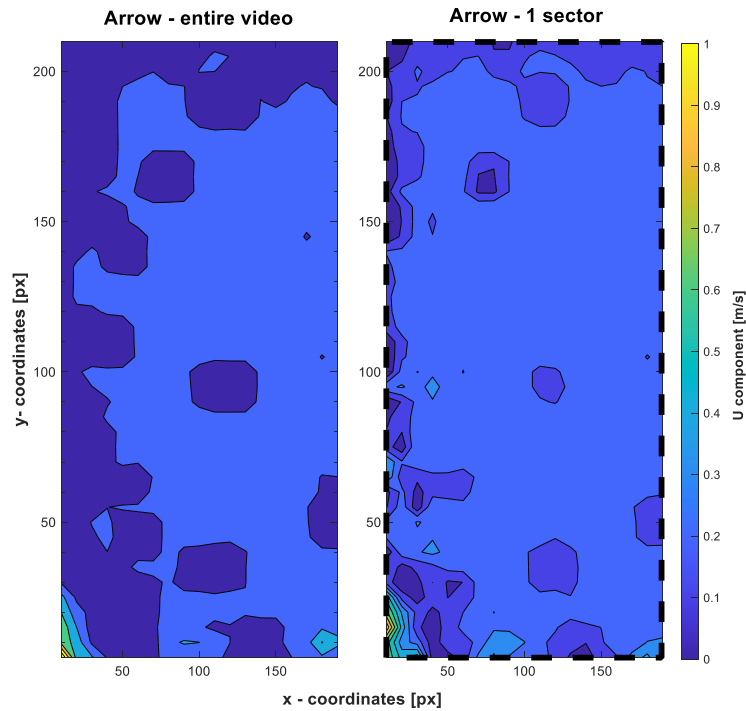
394
395   *Figure 8. Averaged surface velocity map computed for Arrow river inside the ROI considering the entire video and the one sector configuration.*

5 Discussion

The accuracy of image velocimetry techniques strongly depends on the occurrence of visible features (e.g., boils, surface ripples, vegetation debris) on the water surface. In a natural environment, the amount, spatial distribution, and visibility of natural features at the river surface are continuously changing because of environmental factors (reflections, shadows, wind, rain) and hydraulic conditions (water ripples, hydraulic jumps, and standing waves). For this reason, the actual seeding in the field is not always properly captured by the post-processed images (Dal Sasso et al., 2020). In practice, tracers may vary in amount, organisation, and even presence/absence during field experiments or natural conditions. Therefore, operators frequently add traceable particles to increase the accuracy and reliability of the surface velocity measurements. However, also in this case, floating natural particles could not cover the entire observed cross-section, leading to data gaps or near-zero velocities (e.g., typically near the banks).

To avoid these issues and answer to these practical difficulties, in this work a method based on an SDI threshold is proposed to define the best seeding conditions inside a frame sequence. This approach uses only the frames with an SDI below a given threshold, reducing the investigation scale at sub-sectors to maximise this information. The method was applied to different case studies characterised by different lengths of videos and specific seeding conditions in space and time. The SDI-based method improved LSPIV performance with a reduction of image velocimetry errors ranging between 2 and 39% depending on the variability of SDI time series along the frame sequence. These improvements are even more evident at sub-sector scales, when a different seeding behaviour was observed, allowing the possibility to select frames with tracers continuously visible across the ROI. At this scale, a significant reduction of error, between 24 and 33%, was found on the Brenta and Noce rivers respectively. The application of the method at the sector and

419 sub-sector scales allowed a full velocity map to be obtained with a significant reduction in

420 computational time for the analysis, reducing the number frames processed. Moreover, in such

421 cases, the average surface velocity maps contain details (e.g., velocity fluctuations and

422 divergences) that are not visible and appreciable in the entire video configuration (see, i.e., Brenta

423 and Noce case studies, on RH and LH sectors respectively). The empirical parameter

424 $\tau = \rho_{cD*1} D^{*0.1}$ calibrated on three case studies could be particularly useful to derive SDI thresholds

425 and the best frame window from the unique information on seeding density. On average, this

426 parameter stabilised around 0.002 ppp in the circumstances in which seeding was visible inside

427 the ROI and tended to increase for videos only when tracers were not observable. Comparing the

428 LSPIV results with reference measurements in all the case studies, the mean absolute average error

429 computed was around 8-10%. Except for the Brenta where a systematic overestimation of

430 velocities was found, in general, LSPIV results tend to underestimate surface flow velocities,

431 especially for the areas close to the river banks, where fewer tracers were observed.

432 The SDI threshold can represent an efficient method for searching the best frame window to

433 analyse within the video footage. This is feasible when the number of frames inside the FW

434 identified is adequate to perform analysis with enough vector samples. This information is strongly

435 related to the effective seeding detected by the image velocimetry technique, and its recognition is

436 particularly critical in low seeding conditions. A high number of uniformly distributed particles

437 allows a reduction in the number of frames to analyse; on the contrary, a low seeding density

438 requires a higher number of frames to obtain consistent improvements and full surface velocity

439 maps (e.g. the Bradano river).

440 The proposed method could be particularly useful for analysing a long sequence of frames or

441 multiple videos recorded from a fixed monitoring station, facilitating the generation of time series

442   for image velocimetry analysis. One of the most important limitations of the image velocimetry

443   techniques, especially for traditional correlation-based methods, is the computational time. The

444   detection of the best frame window can minimise the number of frames to analyse, reducing

445   computational loads. The latter can be extremely useful for gauge-cams that can directly process

446   the images in situ without the occurrence of additional drives for storing image sequences (Tosi et

447   al., 2020). Moreover, the application of the method at a local scale can be particularly suited for

448   image velocimetry analysis of flood events where the best seeding conditions are particularly

449   challenging. Its application can be interesting at large rivers in which seeding is generally sparse

450   and completely absent for long frame sequences. More sectors would be identified in these cases

451   to specify image velocimetry analysis only inside the best frame windows. It is worth noting that

452   numerous water reflections appearing as tracers in the field of view represent one of the most

453   important factors that can negatively influence the use of the SDI methods. An increase of apparent

454   seeding density and the reduction of the SDI index can strongly affect image velocimetry results,

455   producing erroneous reconstructions of the flow field. This issue can be frequent in natural

456   environments where the conditions are challenging and could be alleviated through extensive

457   image pre-processing. A greater effort is necessary in this direction in our vision, identifying a set

458   of strategies to automatically discriminate tracers from water reflections and environmental noise

459   in natural settings.

460   ## 6 Conclusion

461   In this work, a novel method for the identification of the optimal spatial structure of tracers was

462   introduced to strengthen surface velocity estimation in natural rivers. The approach uses a

463   threshold for selecting the best frame window (FW) based on the SDI values. SDI time series were

464   calculated at the sector and sub-sector scales of each cross-section in order to investigate the scale

465   impact on the proposed seeding metrics. Analyses highlighted that the proposed procedure might

466   improve the overall LSPIV results with an average reduction of velocity errors of between 20%

467   and 39%. Moreover, we observed that the seeding density's calibrated thresholds remain relatively

468   stable around a value of 0.002 ppp, which can be used as a reference quality measure of an image

469   containing tracers. This value was, in fact, successfully applied to the validation study case of the

470   River Arrow.

471   The method appears suitable for natural settings where environmental and hydraulic conditions

472   are extremely challenging and particularly useful for real-time implementations on gauge-cams,

473   where a vast number of frames is usually recorded and analysed. Reducing the observation scale

474   for image velocimetry analysis is a novel idea, successfully explored in this work that reveals a

475   high potential for applying other image velocimetry techniques. In future, this method will be

476   tested on other case studies considering additional seeding configurations and environmental

477   conditions.

478

482   **Code availability statement**

483   The code used to define the best frame window is available at https://doi.org/

484   10.17605/OSF.IO/3AJNR (Dal Sasso et al., 2021). The code used to compute the SDI index as

485   well as seeding metrics is available at https://doi.org/10.17605/OSF.IO/8EGQW.

486

487 **Data availability statement**

488 The data that support the findings of this study are openly available in 4TU.Centre for Research

489 Data at https://doi.org/10.4121/uuid:014d56f7-06dd-49ad-a48c-2282ab10428e (Perks, et al.,

490 2020).

491

492 # References

493 Bandini F, Lüthi B, Peña-Haro S, Borst C, Liu J, Karagkiolidou S, Hu X, Lemaire GG, Bjerg PL, Bauer-Gottwein P 2020. A drone-

494 borne method to jointly estimate discharge and Manning's roughness of natural streams. Water Resources Research.

495 (https://agupubs.onlinelibrary.wiley.com/doi/10.1029/2020WR028266).

496 Boursicaud R, Pénard L, Hauet A, Thollet F, Le Coz J 2016. Gauging Extreme Floods on YouTube: Application of LSPIV to Home

497 Movies for the Post-Event Determination of Stream Discharges. Hydrological Processes. doi:10.1002/hyp.10532.

498 Brevis W, Niño Y, Jirka GH 2011. Integrating cross-correlation and relaxation algorithms for particle tracking velocimetry. Exp.

499 Fluids, 50, 135–147.

500 Dal Sasso SF, Pizarro A, Samela C, Mita L, Manfreda S 2018. Exploring the Optimal Experimental Setup for Surface Flow

501 Velocity Measurements Using PTV. Environmental Monitoring and Assessment 190(8). doi:10.1007/s10661-018-6848-3.

502 Dal Sasso SF, Pizarro A, Manfreda S. 2020. Metrics for the quantification of seeding characteristics to enhance image velocimetry

503 performance in rivers. Remote Sensing DOI: 10.3390/rs12111789.

504 Dal Sasso SF, Pizarro A, Pearce S, Maddock I, Manfreda S. 2021. Increasing LSPIV performances by exploiting the seeding

505 distribution index at different spatial scales (Version 0.1). [codes] OSF. https://doi.org/ 10.17605/OSF.IO/3AJNR.

506 Detert M, Johnson E D, Weitbrecht V 2017. Proof-of-concept for low-cost and non-contact synoptic airborne river flow

507 measurements. Int. J. Remote Sens., 38, 2780–2807.

508 Eltner A, Sardemann H, Grundmann J. 2020. Technical Note: Flow velocity and discharge measurement in rivers using terrestrial

509 and unmanned-aerial-vehicle imagery. Hydrology and Earth System Sciences 24.

510 Fujita I, Muste M, Kruger A 1998. Large-scale particle image ve-locimetry for flow analysis in hydraulic engineering applications,

511   J. Hydraul. Res., 36, 397–414.

512   Fujita I, Watanabe H, Tsubaki R 2007. Development of a non-intrusive and efficient flow monitoring technique: The space-time
513   image velocimetry (STIV), Int. J. River Basin Manage., 5, 105–114.

514   Herschy R W. 1985. Streamflow measurement, Elsevier Applied Science Publishers.

515   Kim Y, Muste M, Hauet A, Krajewski WF, Kruger A, Bradley A 2008. Stream discharge using mobile large-scale particle image
516   velocimetry: A proof of concept, Water Resour. Res., 44, W09502, doi:10.1029/2006WR005441.

517   Kinzel PJ, Legleiter CJ 2019. sUAS-Based Remote Sensing of River Discharge Using Thermal Particle Image Velocimetry and
518   Bathymetric Lidar. Remote Sensing 11 (19): 2317.

519   Le Coz J, Hauet A, Pierrefeu G, Dramais G, Camenen B 2010. Performance of image-based velocimetry (LSPIV) applied to flash-
520   flood discharge measurements in Mediterranean rivers. Journal of Hydrology. https://doi.org/10.1016/j.jhydrol.2010.05.049.

521   Leitão JP, Peña-Haro S, Lüthi B; Scheidegger A, de Vitry M M 2018. Urban overland runoff velocity measurement with consumer-
522   grade surveillance cameras and surface structure image velocimetry. J. Hydrol, 565, 791–804.

523   Manfreda S, Dvorak , J. Mullerova, S. Herban, P. Vuono, J.J. Arranz Justel, M. Perks, 2019°. Assessing the Accuracy of Digital
524   Surface Models Derived from Optical Imagery Acquired with Unmanned Aerial Systems, Drones, 3(1),15; (doi:
525   10.3390/drones3010015).

526   Manfreda S, Dal Sasso SF, Pizarro A, Tauro F 2019b. New Insights Offered by UAS for River Monitoring. In Applications of Small
527   Unmanned Aircraft Systems: Best Practices and Case Studies.

528   Manfreda S, McCabe MF, Miller PE, Lucas R, Madrigal VP, Mallinis G, Dor E Ben, Helman D, Estes L, Ciraolo G, et al. 2018. On
529   the use of unmanned aerial systems for environmental monitoring. Remote Sensing DOI: 10.3390/rs10040641.

530   Muste M, Fujita I, Hauet A 2008. Large-scale particle image velocimetry for measurements in riverine environments. Water
531   Resources Research. https://doi.org/10.1029/2008WR006950

532   Pearce S, Ljubičić R, Peña-Haro S, Perks M, Tauro F, Pizarro A, Dal Sasso S, Strelnikova D, Grimaldi S, Maddock I, et al. 2020.
533   An Evaluation of Image Velocimetry Techniques under Low Flow Conditions and High Seeding Densities Using Unmanned
534   Aerial Systems. Remote Sensing DOI: 10.3390/rs12020232.

535   Perks MT, Dal Sasso SF, Hauet A, Jamieson E, Le Coz J, Pearce S, Peña-Haro S, Pizarro A, Strelnikova D, Tauro F, et al. 2020a.

536   Towards harmonisation of image velocimetry techniques for river surface velocity observations. Earth System Science Data

537   12 (3): 1545–1559 DOI: 10.5194/essd-12-1545-2020.

538   Perks M, Sasso SF (Silvano FD, Detert M (Martin), Hauet A (Alexandre), Jamieson E (Elizabeth), Coz J (Jérôme) Le, Pearce S

539   (Sophie), Peña-Haro S (Salvador), Pizarro A (Alonso), Strelnikova D, et al. 2020b. Data on the harmonization of image

540   velocimetry techniques, from seven different countries, [dataset], DOI: 10.4121/uuid:014d56f7-06dd-49ad-a48c-

541   2282ab10428e.

542   Perks M T 2020. KLT-IV v1.0: image velocimetry software for use with fixed and mobile platforms, Geosci. Model Dev., 13, 6111–

543   6130, https://doi.org/10.5194/gmd-13-6111-2020.

544   Pizarro A, Dal Sasso SF, Manfreda S 2020a. Refining image-velocimetry performances for streamflow monitoring: Seeding metrics

545   to errors minimisation, Hydrological Processes, (doi: 10.1002/hyp.13919), 1-9, 2020a.

546   Pizarro A, Dal Sasso SF, Perks M, Manfreda S 2020b. Identifying the optimal spatial distribution of tracers for optical sensing of

547   stream surface flow, Hydrology and Earth System Sciences, 24, 5173–5185, (10.5194/hess-24-5173-2020) 2020d.

548   Rozos E, Dimitriadis P, Mazi K, Lykoudis S, Koussis A 2020. On the Uncertainty of the Image Velocimetry Method Parameters.

549   Hydrology 2020, 7, 65.

550   Samarage CR, Carberry J, Hourigan K, Fouras A. 2012. Optimisation of temporal averaging processes in PIV. Experiments in

551   Fluids DOI: 10.1007/s00348-011-1080-8

552   Strelnikova D, Paulus G, Käfer S, Anders K-H, Mayr P, Mader H, Scherling U, Schneeberger R. 2020. Drone-Based Optical

553   Measurements of Heterogeneous Surface Velocity Fields around Fish Passages at Hydropower Dams. Remote Sensing

554   Tauro F, Tosi F, Mattoccia S, Toth E, Piscopia R, Grimaldi S 2020. Optical tracking velocimetry (OTV): leveraging optical flow and

555   trajectory-based filtering for surface streamflow observations, Remote Sensing, 10, 2010,

556   https://doi.org/10.3390/rs10122010, 2018.

557   Tauro F, Piscopia R, Grimaldi S 2017. Streamflow Observations From Cameras: Large-Scale Particle Image Velocimetry or Particle

558   Tracking Velocimetry? Water Resour. Res. 2017, 53, 10374–10394. DOI: 10.3390/rs12030384.

559   Thielicke W, Stamhuis EJ. 2014. PIVlab – Towards User-friendly, Affordable and Accurate Digital Particle Image Velocimetry in

560   MATLAB. Journal of Open Research Software DOI: 10.5334/jors.bl.

561   Tosi F, Rocca M, Aleotti F, Poggi M, Mattoccia S, Tauro F, Toth E, Grimaldi S 2020. Enabling Image-Based Streamflow Monitoring
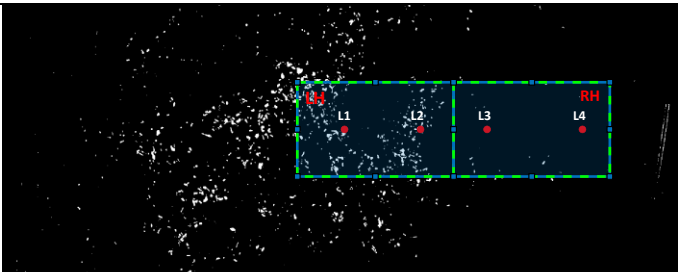
562   at the Edge. Remote Sens. 2020, 12, 2047.

563

564 **Supplemental material**

565 **Appendix A**

566 *Table A1. LSPIV results for each location compared to reference measurements at sector and sub-sectors scale on the Brenta River.*

Brenta river						
FW	Sectors	Locations	U [m/s]	LSPIV velocity [m/s]	Relative error [%]	APE [%]
1-2500	1	L 1	0.46	0.52	14.42	14.42
		L 2	0.45	0.50	12.18	12.18
		L 3	0.31	0.37	19.46	19.46
		L 4	0.32	0.35	10.98	10.98
1420-1573	1	L 1	0.46	0.50	10.07	10.07
		L 2	0.45	0.47	4.45	4.45
		L 3	0.31	0.41	30.15	30.15
		L 4	0.32	0.35	10.98	10.98
1420-1573	2 - LH	L 1	0.46	0.50	10.07	10.07
		L 2	0.45	0.47	4.45	4.45
501-879	2 - RH	L 3	0.31	0.38	21.79	21.79
		L 4	0.32	0.34	7.19	7.19

567
568

569   *Table A2. LSPIV results for each location compared to reference measurements at sector and sub-sectors scale on the Noce River.*
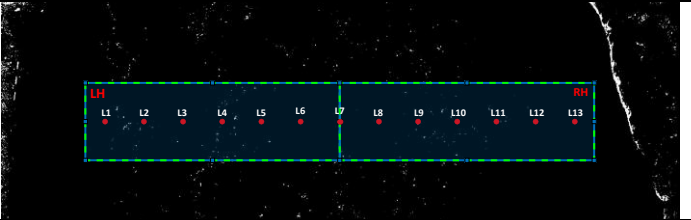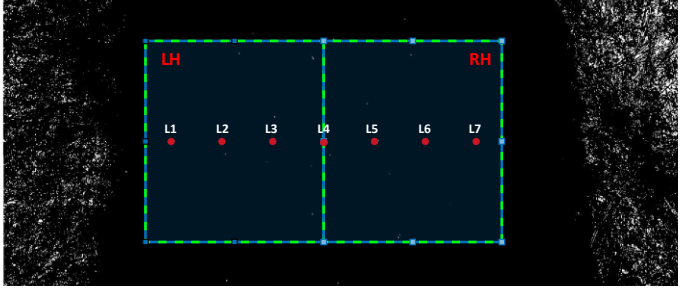
570

FW	Sector	Locations	U [m/s]	LSPIV velocity [m/s]	Relative error [%]	APE [%]
				Noce river		
1-201	1	L 1	0.25	0.19	-21.99	21.99
		L 2	0.38	0.43	13.69	13.69
		L 3	0.47	0.24	-48.70	48.70
		L 4	0.44	0.48	10.05	10.05
		L 5	0.48	0.43	-10.83	10.83
		L 6	0.48	0.40	-16.38	16.38
		L 7	0.46	0.46	0.19	0.19
		L 8	0.47	0.53	11.83	11.83
		L 9	0.48	0.54	10.87	10.87
		L 10	0.47	0.45	-4.43	4.43
		L 11	0.44	0.46	5.09	5.09
		L 12	0.42	0.31	-26.80	26.80
		L 13	0.34	0.33	-4.78	4.78
52-201	1	L 1	0.25	0.19	-21.99	21.99
		L 2	0.38	0.43	13.69	13.69
		L 3	0.47	0.42	-10.94	10.94
		L 4	0.44	0.49	10.72	10.72
		L 5	0.48	0.43	-10.83	10.83
		L 6	0.48	0.34	-29.47	29.47
		L 7	0.46	0.47	1.70	1.70
		L 8	0.47	0.51	8.12	8.12
		L 9	0.48	0.53	10.67	10.67
		L 10	0.47	0.45	-4.43	4.43
		L 11	0.44	0.46	5.09	5.09
		L 12	0.42	0.31	-26.80	26.80
		L 13	0.34	0.33	-4.78	4.78
130-201	2-LH	L 1	0.25	0.19	-21.99	21.99
		L 2	0.38	0.40	6.79	6.79
		L 3	0.47	0.47	0.38	0.38
		L 4	0.44	0.48	9.37	9.37

		L 5	0.48	0.48	-0.53	0.53
		L 6	0.48	0.36	-25.02	25.02
		L 7	0.46	0.49	6.38	6.38
48-186	2-RH	L 7	0.46	0.49	6.38	6.38
		L 8	0.47	0.52	9.85	9.85
		L 9	0.48	0.53	10.01	10.01
		L 10	0.47	0.45	-5.18	5.18
		L 11	0.44	0.43	-1.92	1.92
		L 12	0.42	0.31	-26.80	26.80
		L 13	0.34	0.33	-4.78	4.78

571

572   *Table A3. LSPIV results for each location compared to reference measurements at sector and sub-sectors scale on the Bradano River.*

Bradano river						

FW	Sector	Locations	U [m/s]	LSPIV velocity [m/s]	Relative error [%]	APE [%]
1-2496	1	L 1	0.84	n/a	n/a	n/a
		L 2	1.48	1.29	-12.81	12.81
		L 3	1.04	0.84	-18.82	18.82
		L 4	0.77	0.67	-12.52	12.52
		L 5	0.53	0.48	-9.27	9.27
		L 6	0.43	0.46	7.74	7.74
		L 7	0.63	n/a	n/a	n/a
967-1608	1	L 1	0.84	n/a	n/a	n/a
		L 2	1.48	1.52	2.73	2.73
		L 3	1.04	1.08	3.84	3.84
		L 4	0.77	0.73	-4.95	4.95
		L 5	0.53	0.41	-21.77	21.77
		L 6	0.43	0.49	13.43	13.43
		L 7	0.63	n/a	n/a	n/a
250-1443	2-LH	L 1	0.84	n/a	n/a	n/a
		L 2	1.48	1.39	-6.10	6.10
		L 3	1.04	0.84	-18.82	18.82
1224-1645	2-RH	L 4	0.77	0.72	-6.96	6.96
		L 5	0.53	0.50	-4.73	4.73
		L 6	0.43	0.51	19.14	19.14
		L 7	0.63	n/a	n/a	n/a

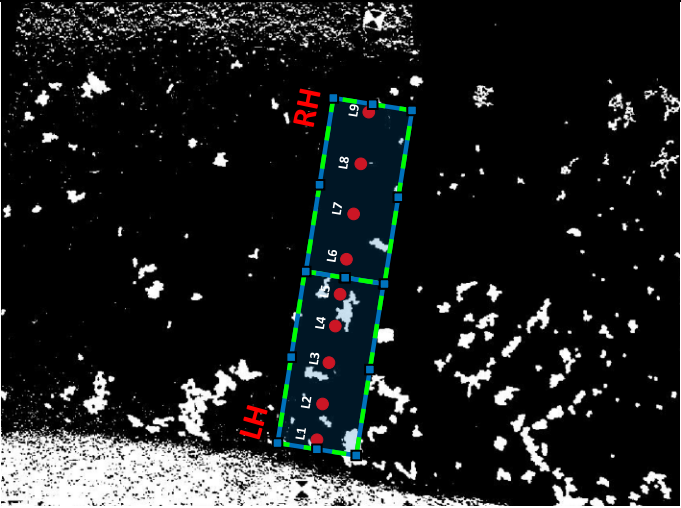573

574

575   *Table A4. LSPIV results for each location compared to reference measurements at sector and sub-sectors scale on the River Arrow.*

576

FW	Sector	Locations	U [m/s]	LSPIV velocity [m/s]	Relative error [%]	APE [%]
1-798	1	L 1	0.099	n/a	n/a	n/a
		L 2	0.25	0.14	-42.33	42.33
		L 3	0.269	0.26	-1.61	1.61
		L 4	0.238	0.27	14.94	14.94
		L 5	0.271	0.26	-5.37	5.37
		L 6	0.18	0.16	-9.66	9.66
		L 7	0.235	0.24	0.42	0.42
		L 8	0.169	n/a	n/a	n/a
		L 9	0.154	n/a	n/a	n/a
195-476	1	L 1	0.099	n/a	n/a	n/a
		L 2	0.25	0.27	7.17	7.17
		L 3	0.269	0.26	-2.04	2.04
		L 4	0.238	0.26	11.24	11.24
		L 5	0.271	0.26	-5.57	5.57
		L 6	0.18	0.21	15.26	15.26
		L 7	0.235	0.22	-4.28	4.28
		L 8	0.169	n/a	n/a	n/a
		L 9	0.154	n/a	n/a	n/a
206-475	2- LH	L 1	0.099	n/a	n/a	n/a
		L 2	0.25	0.27	9.99	9.99
		L 3	0.269	0.27	-0.86	0.86
		L 4	0.238	0.27	13.71	13.71
		L 5	0.271	0.27	-0.69	0.69
262-463	2- RH	L 6	0.18	0.22	21.02	21.02

		L 7	0.235	0.23	-3.37	3.37
		L 8	0.169	n/a	n/a	n/a
		L 9	0.154	n/a	n/a	n/a

577
578
579
580